Probing temperature effects on lattice distortion and oxidation resistance of high-entropy alloys by in situ SR-XRD and XANES

Yuan-Yuan Tan[1,b)], Ming-Yao Su[1,2,b)], Yang-Yang Niu[1,2], Zhou-Can Xie[1,2], Zhong-Jun Chen[3], Yu Gong[3], Jin-Xi Chen[1,2], Zhong-Hua Wu[3], Hai-Ying Wang[1,2], Peter K. Liaw[4], Lan-Hong Dai[1,2,5,a)]

[1] State Key Laboratory of Nonlinear Mechanics, Institute of Mechanics, Chinese Academy of Sciences, Beijing 100190, People's Republic of China
[2] School of Engineering Science, University of Chinese Academy of Sciences, Beijing 100049, People's Republic of China
[3] Institute of High Energy Physics, Chinese Academy of Sciences, Beijing 100049, People's Republic of China
[4] Department of Materials Science and Engineering, The University of Tennessee, Knoxville, TN 37996, USA
[5] State Key Laboratory of Explosion Science and Technology, Beijing Institute of Technology, Beijing 100081, People's Republic of China
a) Address all correspondence to this author. e-mail: lhdai@lnm.imech.ac.cn
b) These authors contributed equally to this paper.

To investigate lattice distortion evolutions of CrCoNi medium-entropy alloy (MEA), CrFeCoNi, and CrMnFeCoNi high-entropy alloys (HEAs) with temperature increasing from 300 to 1323 K, we conduct in situ synchrotron-radiation-based X-ray diffraction experiments. Electron backscattering diffraction, energy-dispersive X-ray spectroscopy and X-ray absorption near edge fine structure spectra (XANES) are further carried out to uncover variations of microstructure, morphology and oxidation resistance. Generally, the lattice will expand continuously with temperature increasing, however, the expansion rate is affected by grain growth and oxidation. The oxidation resistance of CrCoNi MEA is slightly higher than CrFeCoNi HEA, and much higher than CrMnFeCoNi HEA. The XANES spectra demonstrate higher oxidation resistance of Ni, Co, and Fe than Cr and Mn. Formation of local short-range order structures around Ni and Co is observed, but no such features are observed around Fe and Mn. The present findings are significant on deepening the understandings of correlations between atomic structure and mechanical properties in advanced HEAs.

Introduction

High-entropy alloys (HEAs) present prominent mechanical properties [1, 2], and thus, attract increasing research enthusiasm for their great potential applications in vast industrial fields [3–5]. The most representative and widely-studied HEAs are CrMnFeCoNi HEA systems [6–10], including the equiatomic CrMnFeCoNi HEA (namely Cantor alloy), CrFeCoNi HEA, and CrCoNi medium-entropy alloy (MEA). It is frequently reported that the mechanical properties of CrMnFeCoNi HEA systems are highly temperature dependent. Specifically, their deformation mode would go through a transition from twinning to dislocation slip or a synergy of the two as temperature increased from cryogenic to high temperature ranges [9, 11–13]. Taking the CrCoNi MEA for instance, its cryogenic mechanical

performance has broken the strength-ductility trade-off and approaches new records [6, 14]. In contrary, their high-temperature performances are unremarkable [15–18]. This trend has surprised the researchers and made them pour extensive efforts to unveil the underlying mechanisms. Subsequently, experiments [9, 15, 19] and computer-based calculations [20–24] presented a decrease of stacking fault energy (SFE) with temperature down to cryogenic ranges. The reporters thus attributed the simultaneous improvement of strength and ductility to the involvement of twinning. Nevertheless, the variations of SFE and twinning might have close correlations with lattice distortion evolutions [25]. However, few works have been reported to interpret the deformation mode transition from the view point of lattice distortion evolutions with temperature [13]. Since the

lattice distortion (such as, lattice expansion, contraction, and local lattice distortion) will evolve as a function of temperature, so does the transformation of deformation modes. Therefore, there must be some correlations among the lattice distortion, mechanical-deformation mechanism, and temperature effect in CrMnFeCoNi HEAs system.

Lattice distortion, more specifically, local lattice distortion has been a long-standing issue in metal alloys [26, 27]. Referring to its significance, local lattice distortion is considered as one of the four core effects of HEAs [2]. Evidently, the structures of HEAs are quite different with traditional alloys, because the atomic species in HEAs are close to equiatomic and locate randomly at the lattice sites of the crystal structure. Thus, the atomic-size misfits and differences in electronic-structures are inevitable in HEAs. Consequently, these differences are supposed to make lattice distortions in HEAs far more complex than that in conventional dilute alloys [28]. More importantly, charge transfer among different alloy component species will take place when alloying into uniform HEAs, which alters the local electronic structures of alloying component species [29, 30]. This alteration in local electronic structure brings difficulty on estimation of atom radius, and thus, makes the quantitative assessment of local lattice distortion in HEAs much more complicated.

One of the frequently-used parameters to assess local lattice distortion in crystals is the Debye–Waller factor (B) [31, 32], which relates to the off-site displacement of atoms from their ideal sites in the lattice structure. Since the Debye–Waller factor could be mathematically linked to the atomic-displacement parameter, U_{iso}, by the following equation [33]:

$$B = 8\pi^2 U_{iso} \tag{1}$$

The atomic-displacement parameter, U_{iso}, represents the average dynamic atomic displacement and possible static displacement of an atom away from its ideal position [32]. Usually, this parameter could be derived from the collected high-quality scattering or diffraction patterns based on a synchrotron or neutron source. Another commonly-used parameter to estimate atomic-radii differences and the averaged lattice distortion is the empirical parameter, δ [34], which has been adopted extensively in efforts to describe phase-change behaviors and lattice distortion of HEAs. It then suggested that the value of δ should surpass 6.6% in a given HEA when it is considered as distorted severely. However, the lattice distortions in the CrMnFeCoNi HEAs system are considered to be not severe according to studies based on X-ray scattering [35, 36]. More recently, Tan et al. [29] proposed an element-specified parameter, δ_i, to quantify the local lattice distortion centered around a given alloying component, i, in HEAs. This parameter is calculated, based on the averaged atomic pair distance between two targeted components from the X-ray absorption fine structure spectrum (XAFS) and

the averaged atom pair distance of the whole lattice from XRD datasets. Using this parameter, the local lattice-distortion centered around one specific alloying element could be described quantitatively.

Temperature is of critical importance on the lattice distortion and deformation mechanisms of HEAs [37]. The deformation-mode transition of HEAs has been frequently reported and verified by the in situ high resolution transmission electron microscope (HRTEM) [11] and in situ neutron scattering measurements [9, 15]. In the cryogenic and low temperature ranges, the involvement of twinning in the deformation process is proposed to improve significantly the mechanical performance of HEAs. In the study of Otto et al. [38], it pointed clearly that deformation twinning could produce a high degree of work hardening by continuously introducing new interfaces and at the same time decreasing the mean free path of dislocations, thus, leading to a significant increase in the ultimate tensile strength. However, dislocation slip dominates the deformation behavior of HEAs when the temperature approaches to room or above ranges, leading to a sharp reduction of yield strength [15, 38]. But the peak values of yield strengths decrease slowly in elevated-temperature ranges [38]. The decrease of SFE with temperature has been proposed as one of the reasons for twinning occurrence. However, the temperature dependence of SFE [21, 39, 40] in alloys has not been well discussed in detail. Undeniably, the value of SFE relates closely to the local lattice structure and its evolution with temperature [40, 41]. However, there are still no clear descriptions on explaining relationships among the strong temperature dependence of SFE and lattice structure and, furthermore, the deformation-mechanism transition. Evidently, this deformation-mechanism transition must have some relationships with lattice structure evolution. There naturally comes to the question that what kind of lattice-structure evolution has triggered this transition during a tensile test. Consequently, the thermal-expansion coefficient and elastic moduli are measured as a function of temperature [42, 43] in attempts to clarify their correlation with mechanical performance. Considering the strong temperature dependence of lattice distortion, our previous investigation [29, 44] demonstrates a dramatic reduction in the lattice distortion of the CrMnFeCoNi HEA systems when temperature decreases from room temperature to 123 K. The evolution of local lattice distortion is in good consistence with that of twinning occurrence and decrease of stacking fault energy. Thus, we propose that reduction of local lattice distortion might be a potential contributor to twinning.

Here, the present work focuses on the lattice-distortion evolutions from 300 to 1323 K. It is a continual and complementary study of our previous in situ low-temperature XRD experiments. We perform in situ SR-XRD experiments on CrCoNi MEA, CrFeCoNi and CrMnFeCoNi HEAs at 300, 573, 873, 1173, and 1323 K under vacuum conditions in Beijing synchrotron

4414

radiation facility (BSRF) at beamline 4B9A. However, diffraction peaks of oxides are observed when temperature reaches 1173 K, which is out of our expectation. Thus, XAFS measurements are further carried out to examine the oxidation state of each individual alloying component after the heat treatment.

Thermal lattice expansion and surface oxidation

Figure 1 shows the XRD patterns of the CrCoNi MEA, CrFeCoNi and CrMnFeCoNi HEAs obtained at 300, 573, 873, 1173, and 1323 K. In Fig. 1a–c, the observed diffraction peaks from all the three alloys are attributed to (111), (200), (220), and (311) planes of a single-phase face-centered-cubic (FCC) structure. The (111) diffraction peaks for all the three alloys show the highest intensity. But the ratio of (111) to (200) peak height for CrMnFeCoNi HEA is stronger than that of the CrCoNi MEA and CrFeCoNi HEA, which illustrates slightly-preferred orientation for the CrMnFeCoNi HEA. When the temperature increased to 573 K, the diffraction peaks shift overall to left low-angle side due to thermal expansion. Nevertheless, the shape

of the peaks changes very little, indicating a minor change of local lattice distortion at this temperature. We thus propose that lattice expansion of the CrMnFeCoNi HEA system takes place more apparently than variations of local lattice distortion at a moderate temperature. As the temperature further increases to 873 K, the peak heights of (111) peaks from the CrCoNi MEA in Fig. 1a and CrFeCoNi HEA in Fig. 1b increase sharply, while that of the CrMnFeCoNi HEA in Fig. 1c shows a slight increase. This phenomenon illustrates that the disorder in (111) directions in the CrCoNi MEA and CrFeCoNi HEA decreases faster than that in the CrMnFeCoNi HEA in the high-temperature range. At 873 K, the peak height ratios of (111) to (220) increases sharply, compared with that at 573 K. Simultaneously, the peak widths of (111) peaks in the CrCoNi MEA and CrFeCoNi HEA become narrower, indicating the growth of crystal grains. This trend indicates that the (111) planes might be favorable for surface oxidation. While the asymmetry of the (111) peak in the CrMnFeCoNi HEA becomes more obvious from 873 to 1173 K. The occurrence of this asymmetry is simultaneous with the observation of the MnO oxide. In the formation of the MnO oxide, Mn in the near surface of the CrMnFeCoNi HEA matrix
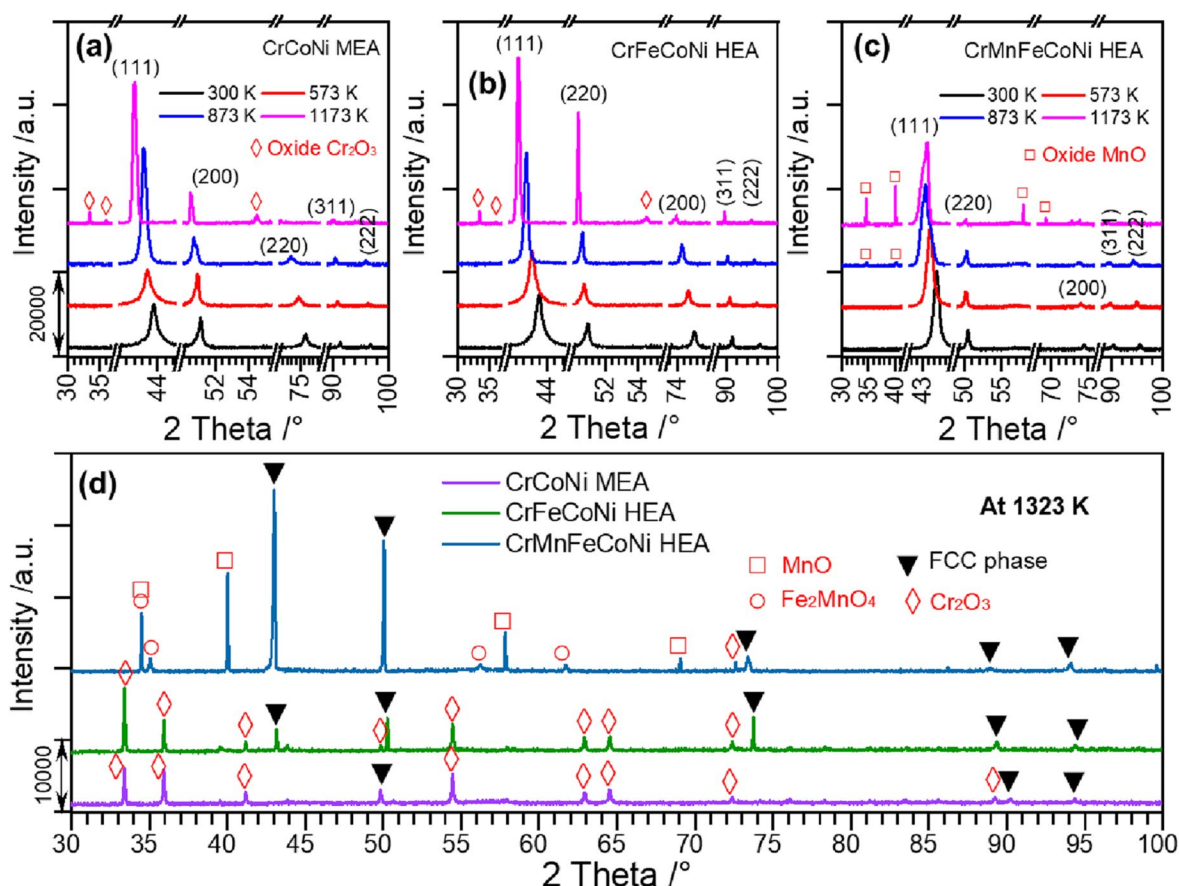

Figure 1: XRD patterns of (a) CrCoNi MEA, (b) CrFeCoNi HEA, and (c) CrMnFeCoNi HEA at 300, 573, 873, and 1173 K collected at the 4B9A beamline in BSRF. The diffraction peaks are expanded at certain angles to make the identification of the peaks easier. The XRD patterns of the three alloys collected at 1323 K are put together in (d) for the ease of comparison.

has to travel to the alloy surface, leading to the increase of the local lattice distortion in the near-surface matrix due to the loss of Mn. Hence, the symmetry of the (111) diffraction peak would decrease as a result of the Mn-outward diffusion.

New diffraction peaks (marked with red square), noticeable but weak, at 34.05° and 40.21° are observed in Fig. 1c, attributing to the formation of MnO (Reference code: 96-154-1155) [45] at the surface of the CrMnFeCoNi HEA. This observation demonstrates a lower oxidation resistance of the CrMnFeCoNi HEA than that of the CrCoNi MEA and CrFeCoNi HEA in the high-temperature range. In contrary to the sharp narrowing of (111) peak width of the CrCoNi MEA and CrFeCoNi HEA, that of CrMnFeCoNi HEA changes very little. Presumably, the diffusions of O, Mn, and Cr take place in priority to the growth of the CrMnFeCoNi HEA crystallite. As the temperature further increases to 1173 K, diffraction peaks of Cr_2O_3 (Reference code: 00-038-1479) [46] are observed clearly in both Fig. 1a and b, verifying oxidation taking place at the surface of the CrCoNi MEA and CrFeCoNi HEA. At 1323 K in Fig. 1d, several diffraction peaks arise from the formed MnO, Cr_2O_3, and Fe_2MnO_4 (Reference code: 96-101-0132) oxides [47]. Simultaneously, the diffraction peaks accounting for the FCC structure in the CrCoNi MEA and CrFeCoNi HEA become very weak. Nevertheless, (111) and (200) diffraction peaks of the CrMnFeCoNi HEA could be observed clearly at this temperature in Fig. 1d. Probably the formed oxidation layers at the surfaces of the CrCoNi MEA and CrFeCoNi HEA are thick and/or dense, which is difficult for X-ray transmission. While X-ray could pass through much easier the oxidation layer at the surface of the CrMnFeCoNi HEA. This phenomenon demonstrates a clear oxidation difference from the CrCoNi MEA and CrFeCoNi HEA to that of the CrMnFeCoNi HEA.

Electron back scattering diffraction (EBSD) images are observed to investigate variations of crystallite sizes after annealing. Figure 2 shows images of grains and size distributions of (a, d) CrCoNi MEA, (b, e) CrFeCoNi HEA, and (c, f) CrMnFeCoNi HEA, respectively. The averaged grain sizes are 71.8, 63.6, and 40.1 μm, which are much larger than those of the original samples (See Fig. S1). The increase of averaged grain size is well consistent with the narrowing of XRD diffraction peaks. The grain size of the CrCoNi MEA is slightly larger than that of the CrFeCoNi HEA and much larger than that of the CrMnFeCoNi HEA, although they were treated in the same condition. This increase of the grain-size order is inverse with their local lattice distortion levels at room temperature: CrMnFeCoNi HEA > CrFeCoNi HEA > CrCoNi MEA [29]. Thus, we propose that higher level of the local lattice distortion is in favor of controlling smaller grain sizes during annealing. This result

Figure 2: EBSD results in the form of inverse pole figure maps of the (a) CrCoNi MEA, (b) CrFeCoNi HEA, and (c) CrMnFeCoNi HEA after in situ XRD measurements at high temperatures. The averaged grain size for (d) CrCoNi MEA, (e) CrFeCoNi HEA, and (f) CrMnFeCoNi HEA are 71.8, 63.6 and 40.1 μm, respectively.
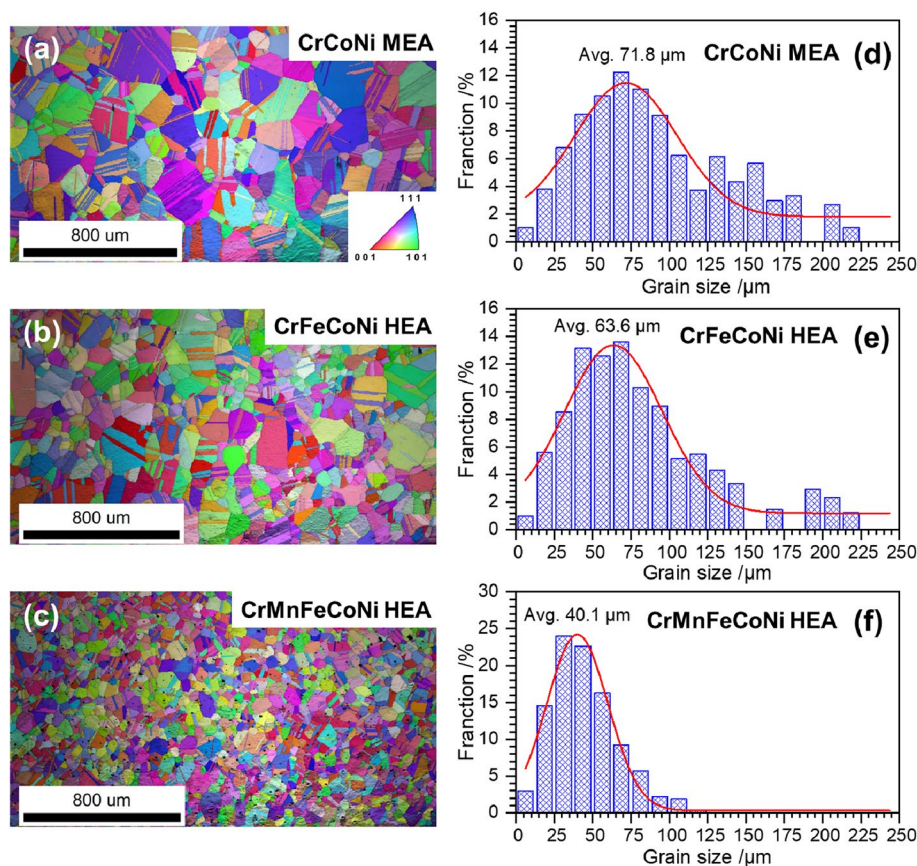
provides critical clues on controlling annealing conditions of CrCoNi MEA, CrFeCoNi and CrMnFeCoNi HEAs.

To investigate surface-oxidation differences among the CrCoNi MEA, CrFeCoNi and CrMnFeCoNi HEAs, scanning electron microscopy (SEM) images and line scan of energy dispersive X-ray spectroscopy (EDS) spectra are collected at the surfaces and cross-sections of the CrCoNi MEA, CrFeCoNi and CrMnFeCoNi HEAs. To enhance the surface conductivity, C in a nano-scale size is sprayed on the surfaces of the samples. The results shown in Fig. 3a and b present a compact oxidation layer at the surfaces of the CrCoNi MEA and CrFeCoNi HEA. This oxidation layer is about 3 μm thick, observed from the cross-section images in Fig. 3d and e, and it consists of mainly Cr and O from the embedded EDS spectra, which is well consistent with the XRD patterns in Fig. 1. Both the surface and cross-section images show that the oxidation layer is compact and attached firmly on the matrix surfaces of the CrCoNi MEA and CrFeCoNi HEA, resulting in the observation of few diffraction peaks from the matrix in the XRD patterns at 1323 K. However, the oxidation surface layer of the CrMnFeCoNi HEA in Fig. 3c is loose and consists of mainly O, Cr, Mn, and Fe from the embedded EDS spectrum, which is quite different from those of the CrCoNi MEA and CrFeCoNi HEA. But in the cross-section image of Fig. 3f, the oxidation surface includes two distinct layers: one is a loose and thick MnO layer in the outside, and another one is a compact and thin Cr_2O_3 layer (about 3 μm) located between the MnO layer and the matrix. We propose that the formation of MnO layer takes place earlier than that of the Cr_2O_3 layer. Because we observe firstly the diffraction peaks from MnO (around 10 μm), and then diffraction peaks from

Cr_2O_3 from the in situ XRD patterns in Fig. 1c. The phenomena illustrate that the outward diffusion of Mn is faster than that of Cr. Otherwise, it would be difficult for Mn to go through a compact Cr_2O_3 oxidation layer. Although the surface oxidation of the CrMnFeCoNi HEA is very different from those of the CrCoNi MEA and CrFeCoNi HEA, the thickness of the Cr_2O_3 oxidation layer for all the three samples are almost the same.

Local lattice-distortion evolutions

The X-ray diffraction data with high quality collected at a synchrotron source could provide detailed microstructural information on the local atomic scale. Hence, lattice distortion could be identified from the refined atomic-displacement parameters. Thus, we further performed Rietveld refinement using the Highscore Plus software [48] to obtain the detailed lattice-distortion-evolution information with increasing temperature. The fitting results are shown in Figs. S2, S3, and S4. After the refinement, lattice-strain evolutions of individual planes are calculated by Eq. (2). During calculations, the lattice parameters obtained at room temperature are used as references.

$$\varepsilon_{(hkl)} = \frac{d_{(hkl)} - d_{(hkl)}^0}{d_{(hkl)}^0} \quad (2)$$

where $\varepsilon_{(hkl)}$ is the lattice strain of (hkl) plane, $d_{(hkl)}$ represents the plane spacing of (hkl) at a given temperature, and $d_{(hkl)}^0$ is the reference plane spacing obtained from XRD patterns collected at room temperature.
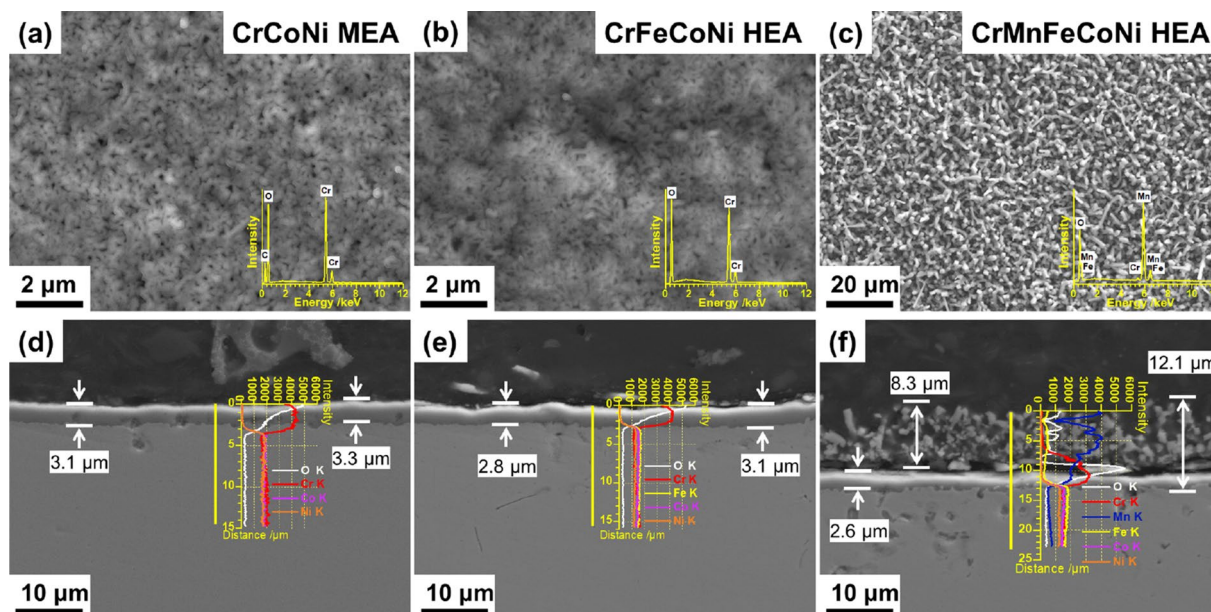

Figure 3: Surface and cross-section morphology of (a, d) CrCoNi MEA, (b, e) CrFeCoNi, and (c, f) CrMnFeCoNi HEAs after oxidation during in situ XRD measurements. The line scan profiles of EDS are also shown in the cross-section morphology images as inserted figures. (The readers are referred to the colors from the online version.).

The refined lattice parameter and lattice strains are shown in Fig. 4. The errors for the lattice parameter, *a*, are generally not larger than 0.0005 Å, thus the error bars are difficult to be identified in Fig. 4a. But a dotted line is presented to connect the error bars. The readers are referred to detailed errors in Table S1 of Supplementary Materials. It presents a general increase of the lattice parameter from the CrCoNi MEA to CrMnFeCoNi HEA at the same temperature in the whole studied temperature range. The lattice parameters of the CrCoNi MEA increases approximately linearly with temperature, but a slight decline is observed from 573 to 873 K due to atom diffusions for the incubation of metal oxides (Cr_2O_3), which is identified in the XRD patterns at higher temperatures in Fig. 1a. Therefore, the formation of Cr_2O_3 at the surface would cause the reduction of the Cr content at the near-surface matrix, which happens to be the probe position of X-ray. Since Cr has the largest atom radius among Cr, Co, and Ni atoms [49], thus the Cr-content reduction will cause the decrease of the lattice parameter of the MEA in the X-ray-detected areas according to Vegard's law [50, 51]. Hence, the expansion rate of the CrCoNi MEA lattice in this temperature range will decrease. As the temperature further increases to 1173 K, the outward diffusion of Cr will become difficult and decreasing due to the formation of a compact oxide layer at the surface. The lattice-parameter evolution of the CrFeCoNi HEA behaves in an approximately-linear increment. No obvious decline of the expansion rate is observed. This trend might

be because of its low Cr concentration, compared with that of the CrCoNi MEA.

Surprisingly, the lattice parameter of the CrMnFeCoNi HEA grows much faster than that of CrCoNi MEA and CrMnFeCoNi HEA from 300 to 573 K, and then its growth rate decreases from 573 to 1173 K. At this temperature range, the loss of atoms with larger atom radii (Mn and Cr) causes the decrease of the lattice of the CrMnFeCoNi HEA, while the continuous heating would expand the lattice. Probably, the outward diffusion effect on the lattice expansion overtakes that of heating, making the lattice expansion decrease for a while. Then, the lattice expansion of the CrMnFeCoNi HEA speeds up as the temperature increases to 1323 K. The acceleration of lattice expansion at this temperature is attributing to the inhibition of Cr and Mn atoms outward diffusions, which is caused by the formation of oxidation layers. The lattice-expansion rates of the CrCoNi MEA and CrFeCoNi HEA are calculated as $(4.11 \pm 0.4) \times 10^{-5}$/K and $(5.42 \pm 0.3) \times 10^{-5}$/K in the temperature range of 300 to 1173 K by linear fitting, respectively. Obviously, the lattice expansion of the CrFeCoNi HEA is faster than that of the CrCoNi MEA, which has similar tendency with their lattice contraction in the low-temperature range according to our previous study [44]. However, the expansion rate of the CrMnFeCoNi HEA might be faster than the CrCoNi MEA and CrFeCoNi HEA if there was no oxidation. Another noticeable feature is that the expansion rate of the lattice is more than 10% higher than their contraction

Figure 4: Evolutions of lattice parameter and strain obtained from the refinement of XRD patterns collected at elevated temperatures. (a) Lattice-parameter evolutions of the CrCoNi MEA (blue), CrFeCoNi HEA (red), and CrMnFeCoNi HEA (purple) with increasing temperature. The dotted lines are the connection of error bars. (b) Lattice strains of individual planes of (111), (200), (220), and (311) in the CrCoNi MEA, CoFeCoNi HEA (c), and CrMnFeCoNi HEA (d). (The readers are referred to the online version of this picture for color indications.).
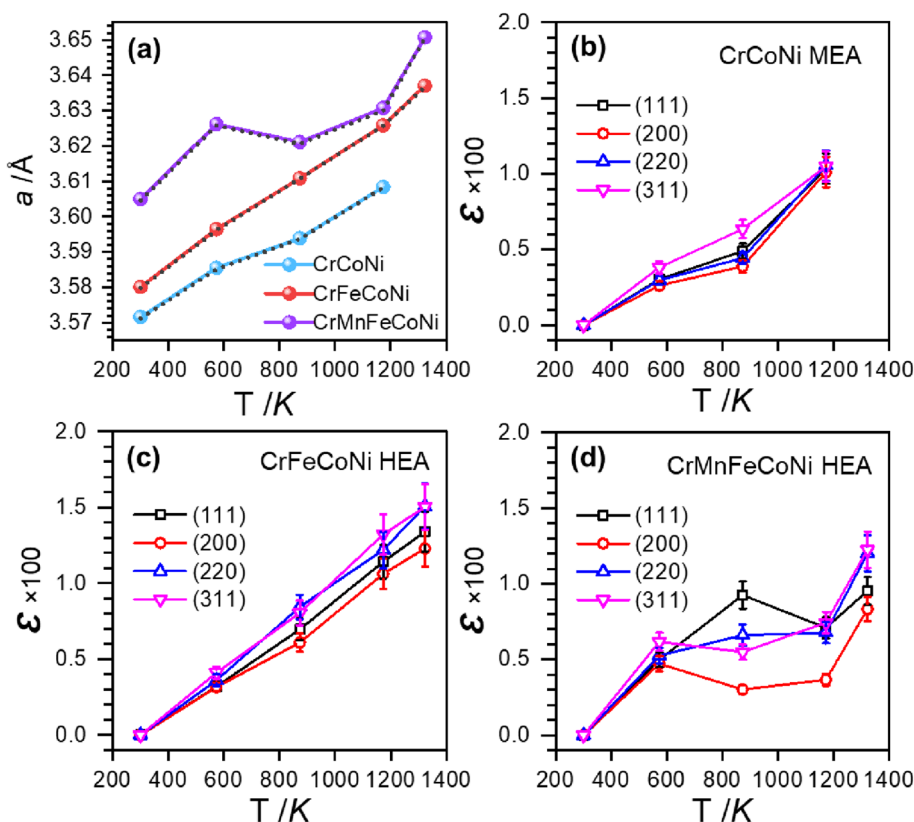
rate in the low-temperature range. Presumably, the enhanced expansion rate is due to violent thermal dynamic oscillations at elevated temperatures. The increasing distances between atom pairs would further reduce attractive forces among atomic bondings, which is favorable for lattice expansion.

The increasing tendency of lattice strains in Fig. 4b–d is well consistent with their lattice parameters in Fig. 4a, but lattice-strain evolutions at different directions within the alloys are heterogeneous from 300 to 1173 K. Generally, (200) planes are the stiffest in the observed planes and show the lowest strains, while (311) planes expand relatively faster in the CrCoNi MEA and CrFeCoNi HEA than that in the CrMnFeCoNi HEA. This small difference is probably caused by the existence of the preferred orientation of (111) in the CrMnFeCoNi HEA. Obviously, the expansions of the alloy lattice are not to the same extent for each individual direction. Thus, the local lattice distortions of the three alloys should have gone through a tremendous diversification in the elevated-temperature range. One aspect is the heterogeneous lattice expansion, and another is the enhanced thermal oscillation with increasing the temperature. However, it is still difficult to make quantitative estimations on the evolution of local lattice-distortion levels. The lattice might be relaxed at higher temperatures, thus, reducing the static displacement. On the other hand, the thermal oscillation would be enhanced accordingly with temperature increase, hence, promoting the dynamic displacement. Therefore, we carry out the detailed analysis of the collected XRD patterns to further estimate local lattice-distortion evolutions of the three alloys.

To obtain an overview of local lattice-distortion evolutions of the CrCoNi MEA, CrFeCoNi and CrMnFeCoNi HEAs in a wide temperature range, we further calculate the variations of lattice parameters and isotropic thermal motion factors (U_{iso}) (Fig. 5), based on the collected XRD patterns in a wide-temperature range from 123 to 1173 K by taking into account of the low-temperature XRD data sets. The data in the low-temperature range are derived from our previous works [44]. During the

calculation, the parameters obtained at room temperature are used as references for the ease of comparison. The increment of the lattice parameter, a, in Fig. 5a is discussed separately in four temperature ranges. In the low-temperature range from 123 to 173 K, as magnified in the insert part, the lattice-expansion rates for the three alloys are slower, compared with those in the higher-temperature range. The turning point for the CrCoNi MEA and CrMnFeCoNi HEA takes place at 173 K, while that of the CrFeCoNi HEA starts from room temperature. Presumably, the lower expanding rate before the turning point temperature could be accounted for two reasons. One is the deactivation of atom diffusions at lower temperatures, and another is the increase of atom-repulsion forces resulting from the shortening of atom distances. In the moderate-temperature range from 173 to 573 K, the lattice expansions of the three alloys increase much faster without crystallite growth. However, the expanding rates of the CrCoNi MEA and CrMnFeCoNi HEA decreased from 573 to 873 K due to the crystallite growth and atom diffusions for the incubation of oxides. Nevertheless, the expansion of the CrFeCoNi HEA lattice continues in a linear way, probably due to its lower Cr content. The results demonstrate that the crystallite growth and oxidation have significant effects on lattice expansion at elevated temperatures. But the effect of crystallite growth should be more profound, since oxidation mainly takes place at the surface of the alloys.

The variations of U_{iso} in Fig. 5b are obtained from the Rietveld refinement of the collected XRD patterns. Sharp increases of ΔU_{iso} of all the three studied alloys are observed in the temperature range from 123 to 300 K, indicating a rapid growth of local lattice distortions, including both dynamic and possible static displacements. However, the increasing rates of ΔU_{iso} in the CrCoNi MEA and CrMnFeCoNi HEA slightly decrease, while that of the CrFeCoNi HEA sees a tiny increase when the temperature increases to 573 K. As the temperature further increases to 873 K, the ΔU_{iso} of the CrCoNi MEA and CrMnFeCoNi HEA increases again but the growing rate is not as high

Figure 5: Lattice parameter (a) and isotropic thermal motion factor (b) variations of the CrCoNi MEA, CrFeCoNi and CrMnFeCoNi HEAs from 123 to 1,173 K. The corresponding parameters obtained at room temperature are used as references for the easy comparison. The magnified part of the low-temperature data is inserted in (a).
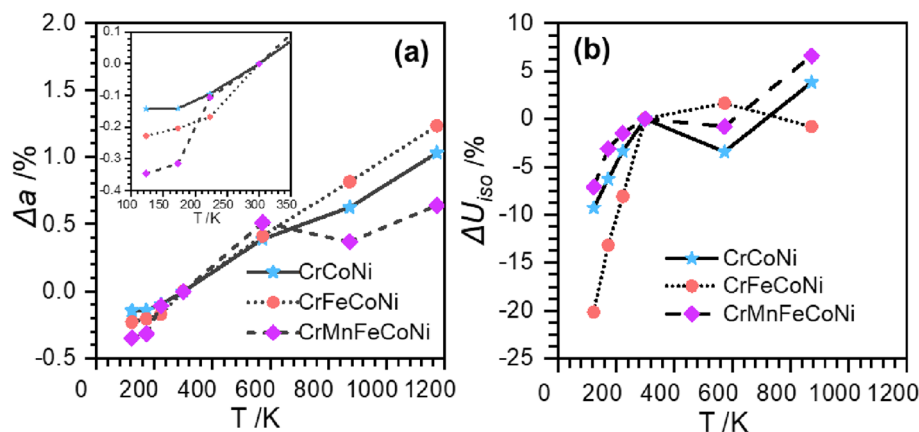
as that below 300 K. Interestingly, the ΔU_{iso} of the CrFeCoNi HEA decreases slightly in this temperature range. These results demonstrate similar variations of ΔU_{iso} of the CrCoNi MEA, CrFeCoNi and CrMnFeCoNi HEAs in the whole studied temperature range, while the deformation-mode transition from twinning at low temperatures to dislocation slip at moderate and higher temperatures for all the three alloys is also similar. This coincidence demonstrates that the local lattice-distortion evolution might be a critical contributor to the transition of the deformation mode for the CrFeCoNi HEA system.

The above results show clearly that the variations of lattice parameters, a, and ΔU_{iso} in the whole studied temperature range are quite different. In particular, a slower increase of the lattice parameter, a, in the low-temperature range is corresponding to a sharp increase of ΔU_{iso}. Whilst a sharp increase of a in the elevated-temperature range (873–1173 K) corresponds to a slow increase of $\Delta U_{iso.}$ The results inform us of that the local lattice-distortion reduction is dominate in the low-temperature range (100–223 K), while lattice expansion suppresses the increase of the local lattice distortion in moderate temperatures (293–573 K). The variations in Fig. 5 illustrate a strong temperature dependence of the local lattice distortion in the low-temperature range (123–223 K), but a relatively-stable level in the high-temperature range (873–1173 K). Thus, it is reasonable to infer that local lattice distortions in CrMnFeCoNi HEA systems mainly arise from dynamic thermal oscillations. Another important supportive aspect is that the effective atomic-size differences among Cr, Mn, Fe, Co, and Ni are not very large [49], and the effective atom-radius misfit of the alloying component should be further reduced when alloying due to charge transferring [29]. The sharp reduction of thermal oscillations at low temperatures makes the atoms in the alloys act more like hard spheres, and easy to be deformed in the way of twinning. However, the thermal oscillation of atoms approaches some limit very quickly in the mediate-temperature range, and lattice expansion together consumes most of the energy received from heating. The enlarged lattice space and enhanced atomic thermal oscillation are more favorable for the activation and slip of dislocations. As the temperature further increases to a higher degree, crystallite growth becomes obvious and takes place in a rapid way. Thus, the lattice structure of the metal alloy goes through tremendous changes in the aspects of local lattice distortion, lattice expansion, and grain-size increase from low to elevated temperatures. It should be noticed that the dominated aspect in the lattice-distortion evolution varies with temperature, which would possibly lead to the deformation-mechanism transition from twinning domination to dislocation slip. It is thus suggested that the local lattice-distortion reduction makes a critical contribution to twinning at low temperatures. While lattice expansion favors the activation and movement of dislocations at mediate and elevated temperatures. However, the rapid growth of crystallites must be taken into account when discussing deformation mechanisms at elevated temperatures.

Oxidation state and local short-range-order structure formation

The surface oxidation has significant effects on the crystallite growth in the near-surface region of the alloys. To explore the oxidation state of each individual element in the CrCoNi MEA, CrFeCoNi and CrMnFeCoNi HEAs, we further measures X-ray absorption near edge spectra (XANES) from K-edges of alloying components (excluding Cr) after in situ XRD measurements. The XANES data are analyzed by a Demeter software package [52]. For ease of comparison, the XANES spectra from K edges of Ni, Co, Fe, and Mn of corresponding standard foil samples are collected in the same condition and display in Fig. 6.

In Fig. 6a, the white line peak heights of the XANES spectra from Ni K-edges of the CrCoNi MEA, CrFeCoNi and CrMnFeCoNi HEAs are close but slightly lower than that of the Ni foil. However, no diffraction peaks accounted for the nickel oxide is observed during the whole-temperature range. Hence, this slight decrease is attributed to charge transfer from other alloying components to Ni. A noticeable feature is the pre-edge peak valley (marked with a dashed circle) in the CrCoNi MEA, CrFeCoNi and CrMnFeCoNi HEAs, compared with that of a Ni foil spectrum, and it is more profound for the CrMnFeCoNi HEA. The appearance of pre-edge peak valleys demonstrates local structure changes around Ni in the alloys after in situ high-temperature XRD measurements. Since there is no nickel oxide at the surface, thus, the local atomic changes around Ni are proposed to take place in the matrix instead of oxide layers. Similar white line peak features are observed for Co in Fig. 6b and Fe in Fig. 6c, compared with their corresponding foil samples. No obvious changes are captured in the pre-edge part of the XANES spectra, indicating subtle local structure modifications around Co and Fe during the heat treatment. However, the white line-peak height of the XANES spectrum from the K-edge of Fe in the CrFeCoNi HEA is higher than that of the CrMnFeCoNi HEA in Fig. 6c, demonstrating charge transferring from other elements to Fe in the CrFeCoNi HEA. Compared with the XANES spectrum of a standard Mn foil sample, a sharp increase of a white line-peak height is observed in the XANES spectrum from the Mn K-edge of the CrMnFeCoNi HEA in Fig. 6d, illustrating serious Mn oxidations in the CrMnFeCoNi HEA. This is well consistent with the emergence of diffraction peaks arising from the formation of MnO in the CrMnFeCoNi HEA in Fig. 1d.

To examine local atomic structure variations, the differences of XANES spectra compared with corresponding XANES spectra from the standard foil samples are calculated in Fig. 7. The sharp decrease of the pre-edge peak valley intensity in Fig. 7a

Figure 6: XANES spectra collected from *K*-edges of Ni, Co, Fe, and Mn of (a) CrCoNi MEA, (b) CrFeCoNi, and (c) CrMnFeCoNi HEA after in situ XRD measurements.
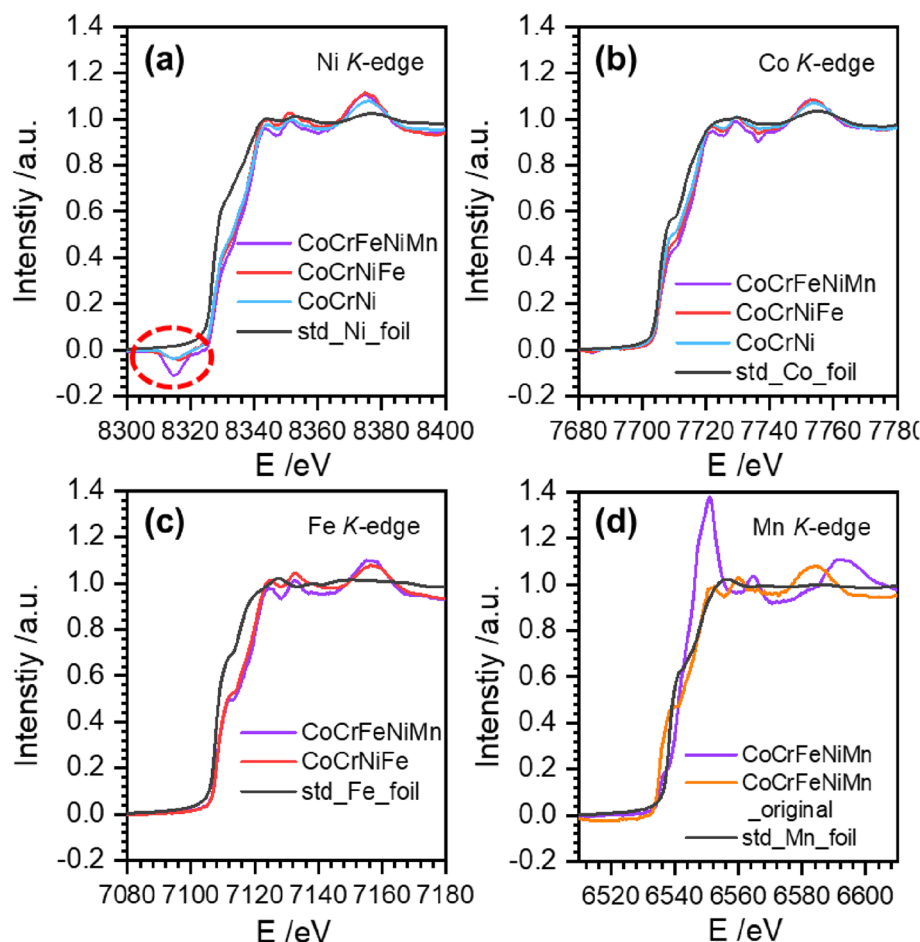

indicates the formation of some short-range local structures around Ni after surface oxidation, and this tendency is more pronounced for the CrMnFeCoNi HEA. A small pre-edge peak increase of the XANES spectra from the Co *K*-edge is conspicuous for the CrCoNi MEA, but no clear feature is shown in the spectra of the CrFeCoNi and CrMnFeCoNi HEAs. This difference demonstrates a short-range order structure conformation around Co in the CrCoNi MEA, but such kind of short-range-order structures do not form in CrFeCoNi and CrMnFeCoNi HEAs. An obvious pre-edge structure feature is not observed in Fig. 7c, demonstrating no formation of some local structures around Fe in CrFeCoNi and CrMnFeCoNi HEAs after heat treatment. However, the white line-peak height of the CrFeCoNi HEA is higher than that of the CrMnFeCoNi MEA. While the white line-peak height of the CrFeCoNi HEA is lower than that of the CrMnFeCoNi HEA without the heat treatment [29]. The increase of the white-line peak height of Fe in the CrFeCoNi HEA reveals a higher oxidation state of Fe than that in the CrMnFeCoNi HEA. Although the peak intensities of the XANES spectra from *K*-edges of Ni, Co, and Fe in the CrCoNi MEA, CrFeCoNi and CrMnFeCoNi HEAs are different, the spectra show similar oscillation shapes after the edges for all the alloys.

This result manifests that these atoms in their alloys keep similar crystal structures but with slight differences in the local short-range environment, which is in well consistent with the XRD results in Fig. 1. However, the difference spectra in Fig. 6d of Mn in the region apart from the edge show obvious phase shifts, indicating that the local atomic structure of Mn has changed dramatically after the heat treatment due to the formation of a Mn oxide.

The XANES spectra and their differences of XRD patterns of the CrCoNi MEA, CrFeCoNi and CrMnFeCoNi HEAs demonstrate clear variations on the oxidation resistance of alloying elements in the three alloys. The Cr and Mn atoms are mostly feasible to be oxidized. Then Fe, Co, and Ni are the last ones to be oxidized at elevated temperatures under low vacuum conditions. This observation is consistent with the formation energy of their corresponding metal oxides. Due to the formation of the Cr and Mn oxides at the surface of the metal, Cr and Mn have diffused outward to the regions near the substrate surface, leading to gradient distributions of Cr and Mn, as shown in Fig. 3. However, the distributions of Ni and Co changed very little for their higher energies on the formation of oxides [53]. Hence, the local short-range-order structure around Ni and Co would be

Figure 7: Differences of XANES spectra from *K*-edges of Ni, Co, Fe, and Mn in the alloys of the CrCoNi MEA, CrFeCoNi and CrMnFeCoNi HEAs after in situ XRD measurements in low vacuum conditions.
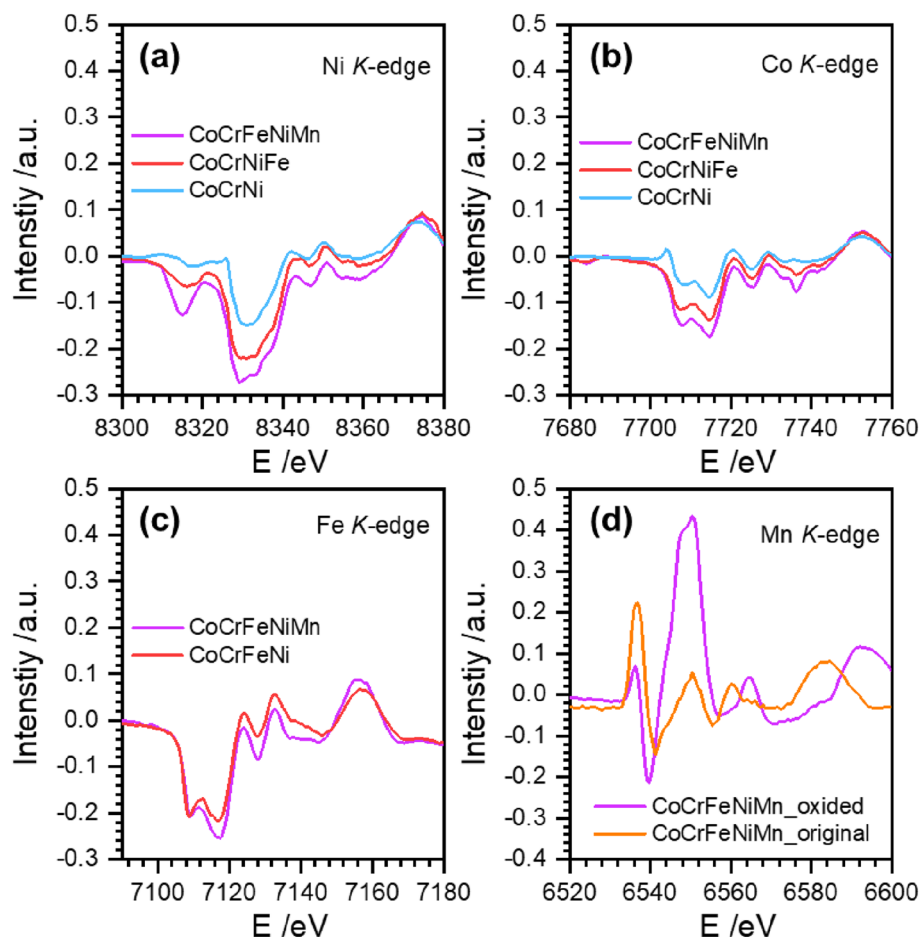
formed as a result of losing Cr, as indicated by the occurrence of their pre-edge valley features in the XANES spectra. As a consequence, the application of the CrMnFeCoNi HEA systems in high-temperature environments should take into considerations of the oxidation and local-structure modifications in the near-surface regions, in particular, for sheet samples. However, the details of the local short-range-order structure variations need to be further studied in the future.

Conclusions

In summary, we carry out in situ SR-XRD experiments to monitor lattice expansion and local lattice variations of the CrCoNi MEA, CrFeCoNi and CrMnFeCoNi HEAs from 300 to 1323 K. Then, EBSD, EDS, and XANES measurements are conducted to investigate variations of the microstructure, morphology, and oxidation property of the three alloys after annealing. We find that the lattices of the CrCoNi MEA, CrFeCoNi and CrMnFeCoNi HEAs expand continuously with the temperature increase, but their expanding rates are different and affected by crystallite growth and oxidation. Under the same annealing condition, the grains of CrCoNi MEA with lower local lattice distortion level grow larger than CrFeCoNi and CrMnFeCoNi HEAs with higher local lattice distortion. Lattice expansion at mediate temperatures favors the reduction of the local lattice distortion, while the oxidation process enhances local lattice distortions at elevated temperatures. Taking the previous in situ low-temperature studies into consideration, we propose that a sharp reduction of the local lattice distortion contributes critically to the strong temperature dependence of deformation mechanisms for the CrMnFeCoNi HEA systems. The oxidation resistance of the CrCoNi MEA and CrFeCoNi HEA is similar and far higher than the CrMnFeCoNi HEA. A compact and thin oxidation layer is found to adhere firmly at the surface of the CrCoNi MEA and CrFeCoNi HEA matrix, while two oxidation layers (one loose and thick outside layer, and one compact and thin inside layer) are observed at the surface of the CrMnFeCoNi HEA. The alloying elements of Cr and Mn are feasible to be oxidized, while Ni and Co are highly oxidation resistant. Short-range-order structures around Ni and Co are formed from the XANES spectra, but such features have not been observed around Fe and Mn components.

Materials and methods

The near-equiatomic CrCoNi MEA, CrFeCoNi and CrMn-FeCoNi HEAs with grains of ~ 20 μm are cut from the same bulk alloys listed in our previous report [29]. Briefly, the ingots are prepared by arc melting for five times and homogenized at 1473 K for 24 h, air cooling, cold rolling, and annealing (1073 K, 1 h) are performed for lattice-distortion investigations. The in situ high-temperature SR-XRD measurements are carried out at the 4B9A beamline station in the Beijing Synchrotron Radiation Facility (BSRF) with an incident X-ray wavelength of 1.5406 Å. The sample is cut in a size of 7 mm × 7 mm × 1 mm and put in a vacuum chamber of the high-temperature furnace (Anton Paar HTK 1200 N). The furnace is mounted at a 6-circle diffractometer. A K-B thermocouple is put in the chamber very close to the sample for the purpose of monitoring the stability of the target temperature and temperature-increase rate (10 K/min). To stabilize the sample temperature during the measurement, a moment of 30 min is kept at the designated temperature before each XRD-pattern collection. The individual XRD pattern is collected from a two-theta angle of 35° to 105° with a scanning step of 0.02°. The collection time for a single XRD pattern is around 2 h. Totally, 15 XRD patterns are collected at 300, 573, 873, 1173, and 1323 K for the CrCoNi MEA, CrFeCoNi and CrMnFeCoNi HEAs, respectively. Although the experiments are conducted in vacuum conditions (0.1 Pa), surface oxidations are observed when the heating temperature arriving at 1173 K. To avoid the effect of beam decaying in a long-time range, all the XRD data have been normalized, using the same method before refinement analysis. The XRD pattern is normalized simply in the way of $\left(I_{collected} / I_{incident} \right) \times 10^5$. Thus, the unit of "Intensity" is arbitrary unit, short as a.u. in the presented XRD patterns in Fig. 1. Standard Si powders are measured at the same time to determine instrument broadening.

After the in situ XRD measurement, the cross-sections of the three samples are polished. The morphologies and elemental compositions of the sample surface and cross-section are observed by scanning electron microscopy (SEM) and energy dispersive X-ray spectroscopy (EDS) using JEOL JSM-7900F under 20 kV with a current of 20 nA. Then the grain size and orientation are characterized by electron backscattering diffraction (EBSD). The scanning step for all the three samples is 3 μm in the EBSD data collection, which is much smaller than the averaged grain size. The OIM Analysis software (EDAX, Mahwah, NJ, version 6.1.2) is used to analyse the EBSD data.

To examine oxidation species at the sample surface, XAFS measurements are performed hereafter high-temperature XRD experiments. The XAFS spectra from the K-edge of each component element of the CrCoNi MEA, CrFeCoNi and CrMnFeCoNi HEAs are obtained in a fluorescence mode, using a Lytle detector at the 4B9A station in BSRF. However, the K-edge XAFS spectra of Cr did not collect due to energy limitations of the beamline station.

Data availability

The datasets in the present work are available upon the reasonable request from the corresponding author.

Declarations

Conflict of interest The authors have no conflicts of interest to declare relating to this article.

Supplementary Information

The online version contains supplementary material available at https://doi.org/10.1557/s43578-021-00419-8.

References

1. B. Cantor, I.T.H. Chang, P. Knight, A.J.B. Vincent, Microstructural development in equiatomic multicomponent alloys. Mater. Sci. Eng. A **375–377**(1–2), 213–218 (2004)

2. J.W. Yeh, S.K. Chen, S.J. Lin, J.Y. Gan, T.S. Chin, T.T. Shun, C.H. Tsau, S.Y. Chang, Nanostructured high-entropy alloys with multiple principal elements: novel alloy design concepts and outcomes. Adv. Eng. Mater. **6**(5), 299–303 (2004)

3. X.F. Liu, Z.L. Tian, X.F. Zhang, H.H. Chen, T.W. Liu, Y. Chen, Y.J. Wang, L.H. Dai, "Self-sharpening" tungsten high-entropy alloy. Acta Mater. **186**, 257–266 (2020)

4. Z. Li, S. Zhao, R.O. Ritchie, M.A. Meyers, Mechanical properties of high-entropy alloys with emphasis on face-centered cubic alloys. Prog. Mater. Sci. **102**(3), 296–345 (2019)

5. E.P. George, D. Raabe, R.O. Ritchie, High-entropy alloys. Nat. Rev. Mater. **4**(8), 515–534 (2019)

6. B. Gludovatz, A. Hohenwarter, D. Catoor, E.H. Chang, E.P. George, R.O. Ritchie, A fracture-resistant high-entropy alloy for cryogenic applications. Science **345**(6201), 1153–1158 (2014)

7. J.P. Liu, J.X. Chen, T.W. Liu, C. Li, Y. Chen, L.H. Dai, Superior strength-ductility CoCrNi medium-entropy alloy wire. Scr. Mater. **181**, 19–24 (2020)

8. F.H. Cao, Y.J. Wang, L.H. Dai, Novel atomic-scale mechanism of incipient plasticity in a chemically complex CrCoNi medium-entropy alloy associated with inhomogeneity in local chemical environment. Acta Mater. **194**, 283–294 (2020)

9. M. Naeem, H. He, F. Zhang, H. Huang, S. Harjo, T. Kawasaki, B. Wang, S. Lan, Z. Wu, F. Wang, Y. Wu, Z. Lu, Z. Zhang, C.T. Liu, X.L. Wang, Cooperative deformation in high-entropy alloys at ultralow temperatures. Sci. Adv. **6**(13), eaax4002 (2020)

10. Z. Li, K.G. Pradeep, Y. Deng, D. Raabe, C.C. Tasan, Metastable high-entropy dual-phase alloys overcome the strength-ductility trade-off. Nature **534**(7606), 227–230 (2016)

11. Q. Ding, X. Fu, D. Chen, H. Bei, B. Gludovatz, J. Li, Z. Zhang, E.P. George, Q. Yu, T. Zhu, R.O. Ritchie, Real-time nanoscale observation of deformation mechanisms in CrCoNi-based medium- to high-entropy alloys at cryogenic temperatures. Mater. Today **25**(5), 21–27 (2019)

12. M. Schneider, G. Laplanche, Effects of temperature on mechanical properties and deformation mechanisms of the equiatomic CrFeNi medium-entropy alloy. Acta Mater. **204**, 116470 (2021)

13. H.Y. Diao, R. Feng, K.A. Dahmen, P.K. Liaw, Fundamental deformation behavior in high-entropy alloys: an overview. Curr. Opin. Solid State Mater. Sci. **21**(5), 252–266 (2017)

14. T.A.G. Restivo, G.M.G. Restivo, Development of ultra-hard multi-component alloys. J. Mater. Res. 1–12 (2021)

15. W. Woo, E.W. Huang, J.W. Yeh, H. Choo, C. Lee, S.Y. Tu, In-situ neutron diffraction studies on high-temperature deformation behavior in a CoCrFeMnNi high entropy alloy. Intermetallics **62**, 1–6 (2015)

16. N.D. Stepanov, D.G. Shaysultanov, N.Y. Yurchenko, S.V. Zherebtsov, A.N. Ladygin, G.A. Salishchev, M.A. Tikhonovsky, High temperature deformation behavior and dynamic recrystallization in CoCrFeNiMn high entropy alloy. Mater. Sci. Eng. A **636**, 188–195 (2015)

17. N.K. Adomako, J.H. Kim, Y.T. Hyun, High-temperature oxidation behaviour of low-entropy alloy to medium- and high-entropy alloys. J. Therm. Anal. Calorim. **133**(1), 13–26 (2018)

18. H.T. Jeong, H.K. Park, K. Park, T.W. Na, W.J. Kim, High-temperature deformation mechanisms and processing maps of equiatomic CoCrFeMnNi high-entropy alloy. Mater. Sci. Eng. A **756**(1), 528–537 (2019)

19. Q.J. Li, H. Sheng, E. Ma, Strengthening in multi-principal element alloys with local-chemical-order roughened dislocation pathways. Nat. Commun. **10**(1), 1–11 (2019)

20. S. Huang, W. Li, S. Lu, F. Tian, J. Shen, E. Holmström, L. Vitos, Temperature dependent stacking fault energy of FeCrCoNiMn high entropy alloy. Scr. Mater. **108**, 44–47 (2015)

21. S. Zhao, G.M. Stocks, Y. Zhang, Stacking fault energies of face-centered cubic concentrated solid solution alloys. Acta Mater. **134**, 334–345 (2017)

22. Y.H. Zhang, Y. Zhuang, A. Hu, J.J. Kai, C.T. Liu, The origin of negative stacking fault energies and nano-twin formation in face-centered cubic high entropy alloys. Scr. Mater. **130**, 96–99 (2017)

23. X. Zhang, B. Grabowski, F. Körmann, A.V. Ruban, Y. Gong, R.C. Reed, T. Hickel, J. Neugebauer, Temperature dependence of the stacking-fault Gibbs energy for Al, Cu, and Ni. Phys. Rev. B **98**(22), 224106 (2018)

24. Z. Xie, Y. Wang, C. Lu, L. Dai, Sluggish hydrogen diffusion and hydrogen decreasing stacking fault energy in a high-entropy alloy. Mater. Today Commun. **26**(11), 101902 (2021)

25. J. Xiao, N. Wu, O. Ojo, C. Deng, Stacking fault and transformation-induced plasticity in nanocrystalline high-entropy alloys. J. Mater. Res. 1–10 (2021)

26. W.G. Burgers, Lattice distortion in nickel-iron. Nature 1037–1038 (1935)

27. G.W. Brindley, P. Ridley, An X-ray study of lattice-distortion in copper, nickel and rhodium. Proc. Phys. Soc. **51**(3), 432–448 (1939)

28. J. Kaufman, K. Esfarjani, Tunable lattice distortion in MgCoNiCuZnO5 entropy-stabilized oxide. J. Mater. Res. (2021)

29. Y.-Y. Tan, M.-Y. Su, Z.-C. Xie, Z.-J. Chen, Y. Gong, L.-R. Zheng, Z. Shi, G. Mo, Y. Li, L.-W. Li, H.-Y. Wang, L.-H. Dai, Chemical composition dependent local lattice distortions and magnetism in high entropy alloys. Intermetallics **129**(11), 107050 (2021)

30. N. Li, J. Gu, B. Gan, Q. Qiao, S. Ni, M. Song, Effects of Mo-doping on the microstructure and mechanical properties of CoCrNi medium entropy alloy. J. Mater. Res. **35**(20), 2726–2736 (2020)

31. E.S.K. Menon, A.G. Fox, On the determination of the Debye-Waller factor and structure factors of NiAl by X-ray powder diffraction. Acta Mater. **44**(6), 2547–2555 (1996)

32. K.N. Trueblood, H.B. Bürgi, H. Burzlaff, J.D. Dunitz, C.M. Gramaccioli, H.H. Schulz, U. Shmueli, S.C. Abrahams, Atomic displacement parameter nomenclature report of a subcommittee on atomic displacement parameter nomenclature. Acta Crystallogr. Sect. A **52**(5), 770–781 (1996)

33. D.B. Sirdeshmukh, L. Sirdeshmukh, K.G. Subhadra, *Micro- and Macro-Properties of Solids*, 1st edn. (Springer, Switzerland, 2006)

34. Y. Zhang, Y.J. Zhou, J.P. Lin, G.L. Chen, P.K. Liaw, Solid-solution phase formation rules for multi-component alloys. Adv. Eng. Mater. **10**(6), 534–538 (2008)

35. L.R. Owen, H.J. Stone, H.Y. Playford, The assessment of local lattice strains in alloys using total scattering. Acta Mater. **170**, 38–49 (2019)

36. Y. Tong, K. Jin, H. Bei, J.Y.P. Ko, D.C. Pagan, Y. Zhang, F.X. Zhang, Local lattice distortion in NiCoCr, FeCoNiCr and FeCoNiCrMn concentrated alloys investigated by synchrotron X-ray diffraction. Mater. Des. **155**, 1–7 (2018)

37. B. Fu, W.Y. Yang, L.F. Li, Effect of transformaiton behavior of retained austenite on mechanical properties of cold-rolled TRIP steel. Trans. Mater. Heat Treat. **38**(12), 33–34 (2017)

38. F. Otto, A. Dlouhý, C. Somsen, H. Bei, G. Eggeler, E.P. George, The influences of temperature and microstructure on the tensile properties of a CoCrFeMnNi high-entropy alloy. Acta Mater. **61**(15), 5743–5755 (2013)

39. X. Sun, S. Lu, R. Xie, X. An, W. Li, T. Zhang, C. Liang, X. Ding, Y. Wang, H. Zhang, L. Vitos, Can experiment determine the stacking fault energy of metastable alloys. Mater. Des. **199**, 109396 (2021)

40. H. Van Swygenhoven, P.M. Derlet, A.G. Frøseth, Stacking fault energies and slip in nanocrystalline metals. Nat. Mater. **3**(6), 399–403 (2004)

41. S.F. Liu, Y. Wu, H.T. Wang, J.Y. He, J.B. Liu, C.X. Chen, X.J. Liu, H. Wang, Z.P. Lu, Stacking fault energy of face-centered-cubic high entropy alloys. Intermetallics **93**, 269–273 (2018)

42. G. Laplanche, P. Gadaud, O. Horst, F. Otto, G. Eggeler, E.P. George, Temperature dependencies of the elastic moduli and thermal expansion coefficient of an equiatomic, single-phase CoCrFeMnNi high-entropy alloy. J. Alloys Compd. **623**, 348–353 (2015)

43. G. Laplanche, P. Gadaud, C. Bärsch, K. Demtröder, C. Reinhart, J. Schreuer, E.P. George, Elastic moduli and thermal expansion coefficients of medium-entropy subsystems of the CrMnFeCoNi high-entropy alloy. J. Alloys Compd. **746**, 244–255 (2018)

44. Y.-Y. Tan, M.-Y. Su, Y.-Y. Niu, Z.-C. Xie, Z.-J. Chen, Y. Gong, J.-X. Chen, Z.-H. Wu, H.-Y. Wang, L.-H. Dai, Lattice distortion and magnetic property of high entropy alloys at low temperatures. J. Mater. Sci. Technol. **104**, 236–243 (2022)

45. S. Sasaki, K. Fujino, Y. Takeuchi, X-ray determination of electron density distributions in oxides, MgO, MnO, CoO, and NiO, and atomic scattering factors of their constituent atoms. Proc. Jpn. Acad. **55**(2), 43–48 (1979)

46. M.K. Murthy, F.A. Hummel, X-ray study of the solid solution of TiO, Fe2O3, and G, O3 in mullite (3A12O3a2Si02). J. Am. Ceram. Soc. **43**(5), 267–273 (1960)

47. U. König, G. Chol, Röntgenbeugungs- und Neutronenbeugung-suntersuchungen an Ferriten der reihe MnxZn1−xFe2O4. J. Appl. Crystallogr. **1**(2), 124–126 (1968)

48. T. Degen, M. Sadki, E. Bron, U. König, G. Nénert, The high score suite. Powder Diffr. **29**, S13–S18 (2014)

49. N.L. Okamoto, K. Yuge, K. Tanaka, H. Inui, E.P. George, Atomic displacement in the CrMnFeCoNi high-entropy alloy—a scaling factor to predict solid solution strengthening. AIP Adv. **6**(12), 125008 (2016)

50. E. Zen, Validity of "Vegard's law" 523–524 (1956)

51. A.R. Denton, N.W. Ashcroft, Vegard's law. Phys. Rev. A **43**(6), 1–3164 (1991)

52. B. Ravel, M. Newville, ATHENA, ARTEMIS, HEPHAESTUS: data analysis for X-ray absorption spectroscopy using IFEFFIT. J. Synchrotron Radiat. **12**(4), 537–541 (2005)

53. C. Stephan-Scherb, W. Schulz, M. Schneider, S. Karafiludis, G. Laplanche, High-temperature oxidation in dry and humid atmospheres of the equiatomic CrMnFeCoNi and CrCoNi high- and medium-entropy alloys. Oxid. Met. **95**(1–2), 105–133 (2021)